CHEMISTRY OF MATERIALS

Article

pubs.acs.org/cm

# Electrochemistry of Hollandite $\alpha$-$MnO_2$: Li-Ion and Na-Ion Insertion and $Li_2O$ Incorporation

David A. Tompsett* and M. Saiful Islam*

Department of Chemistry, University of Bath, Bath BA2 7AY, U.K.

**ABSTRACT:** $MnO_2$ is attracting considerable interest in the context of rechargeable batteries, supercapacitors, and Li−$O_2$ battery applications. This work investigates the electrochemical properties of hollandite $\alpha$-$MnO_2$ using density functional theory with Hubbard U corrections (DFT+U). The favorable insertion sites for Li-ion and Na-ion insertion are determined, and we find good agreement with measured experimental voltages. By explicit calculation of the phonons we suggest multiple insertion sites are accessible in the dilute limit. Significant structural changes in $\alpha$-$(Li,Na)_xMnO_2$ during ion insertion are demonstrated by determining the low energy structures. The significant distortions to the unit cell and Mn coordination are likely to be active in causing the observed degradation of $\alpha$-$MnO_2$ with cycling. The presence of $Li_2O$ in the structure reduces these distortions significantly and is the probable cause for the good experimental cycling stability of $\alpha$-$[0.143Li_2O]$-$MnO_2$. However, the presence of $Na_2O$ is less effective in reducing the distortion of the Na-ion intercalated form. We also find a distinct change in the favored Li-ion insertion site, not identified in previous studies, for lithiation of $\alpha$-$Li_xMnO_2$ at $x > 0.5$. The migration barriers for both Li-ions and Na-ions increase from <0.3 eV in the dilute limit to >0.48 eV for $\alpha$-$(Li,Na)_{0.75}MnO_2$. Finally, the electronic density of states in $\alpha$-$MnO_2$ with the incorporation of $Li_2O$ has the character of a full metal, not a half metal as was suggested in previous work. This may be key to its good performance as a catalyst in Li−$O_2$ batteries.

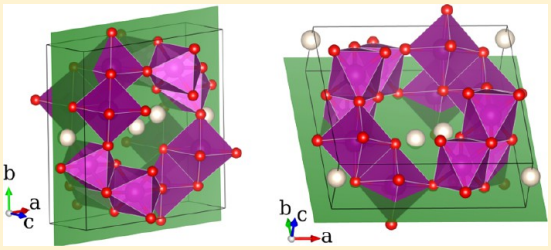


**KEYWORDS:** *lithium battery, sodium battery, DFT, cathode, manganese oxides, $Li_2O$, Li−air*

## 1. INTRODUCTION

Energy storage for hybrid electric vehicles and renewable energy sources are important potential applications for Li-ion and, with renewed interest, Na-ion batteries. Yet the demands of these applications will require cathode materials that perform better and more affordably than the $LiCoO_2$ system conventionally used in rechargeable Li-ion batteries.[1−4] Manganese oxides are a favored class of materials for the future due to their low cost, low toxicity, and superior safety.[5−8]

Electrolytic $MnO_2$, known as EMD, has been an important component of primary alkaline batteries for decades. It is a multiphase material incorporating several polymorphs of $MnO_2$, and whether it possesses intergrowths, microtwinning, and phase mixtures is still under investigation.[9−11] While rutile $\beta$-$MnO_2$ is generally accepted to predominate,[9] EMD also includes other polymorphs and disorder due to the near degeneracy of $\beta$-$MnO_2$ with other structures. The polymorph considered in this work, $\alpha$-$MnO_2$, has also been extensively investigated as a cathode for rechargeable Li-ion cells.[7] Due to key limitations, however, early studies were unable to deliver a rechargeable cell appropriate for commercial use. In $\alpha$-$MnO_2$ the retention of capacity decreased after a few cycles[12] due to structural degradation. Figure 1 shows the unit cell of $\alpha$-$MnO_2$ where the approximate $MnO_6$ octahedra are indicated by polyhedra. In-plane there are both corner- and edge-sharing octahedra forming a 2 × 2 tunnel structure along the *c*-axis. Parallel to the *c*-axis all of the octahedra are edge-sharing, forming a densely packed wall to the tunnel.

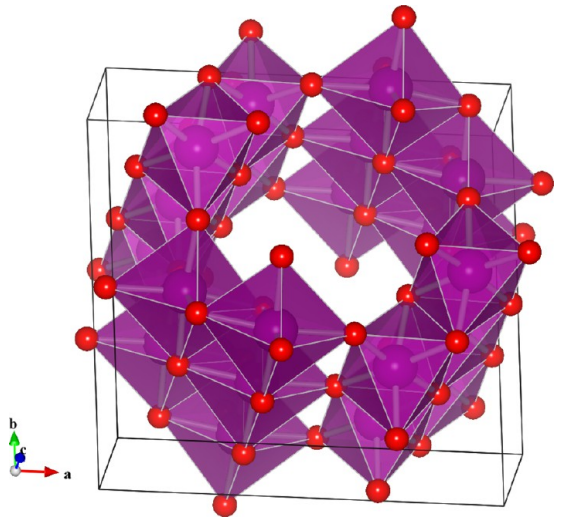


**Figure 1.** Crystal structure of $\alpha$-$MnO_2$. Small (red) spheres are oxygen and large (purple) manganese lie inside the indicated approximate $MnO_6$ octahedra.

Recent work has reinvigorated interest in $\alpha$-$MnO_2$. Stabilizing the structure with $Li_2O$ and ammonia leads to

**Received:** March 18, 2013
**Revised:** May 17, 2013
**Published:** May 22, 2013

   dx.doi.org/10.1021/cm400864n | *Chem. Mater.* 2013, 25, 2515−2526

good cycling at high capacity of 240 mA h $g^{-1}$.[13,14] It is thought that the ammonia can displace any remaining $H_2O$ from synthesis and possibly form $NH_4^+$ that stabilizes the structure further. Nanostructuring of $\alpha$-$MnO_2$ has recently been employed as another route to enhance the electrochemical properties of rechargeable battery electrodes[15−20] giving cathode capacities[16] of 160 mA h $g^{-1}$. Furthermore, Kijima et al.[21] have demonstrated that stabilizing the structure by chemical insertion of two Li-ions per unit cell gives rise to improved initial discharge capacity. These studies make clear the importance of inserted cations for enhancing structural stability during cycling. Stable cycling performance of $\alpha$-$MnO_2$ has been reported by Hill et al.[22] when samples were prepared by hydrothermal−electrochemical synthesis.

Nanostructuring has also been used to improve the performance of $\alpha$-$MnO_2$ in supercapacitors.[23−26] Several experimental studies have reported high capacitance which has been attributed to the strong intercalation properties and high surface area of nanostructured $\alpha$-$MnO_2$. Polymorphic forms of mesoporous $MnO_2$ have also recently shown good supercapacitance.[27] $\alpha$-$MnO_2$ has shown promise as a catalyst for the oxygen reduction reaction that is the basis of the Li−$O_2$ battery system.[28,29] However, whether $\alpha$-$MnO_2$ catalyzes the conversion of lithium peroxide necessary for the Li−$O_2$ battery or in fact enhances electrolyte decomposition requires further investigation.[30,31] This highlights the importance of the fundamental study of $\alpha$-$MnO_2$, and in particular, atomic-scale insights into the structural and thermodynamic changes during Li-ion insertion and $Li_2O$ incorporation.

Historically, research into Li-ion batteries has primarily focused on small devices that require high gravimetric and volumetric capacity. But recent large scale applications such as hybrid electric vehicles and grid storage have also brought Na-ion technology to the forefront of research. This is due to the increased importance of materials abundance (sustainability), cost, and cycle−life performance for larger-scale applications.

Sodium intercalation compounds have been studied for over three decades, for instance, in the $Na_xCoO_2$ cathode,[32] but renewed interest in Na-ion technology has pushed research to consider alternative materials. Sodium insertion into $MnO_2$ has been considered particularly attractive since its crystals form suitably large-sized tunnel structures to accommodate the larger Na ion.[7,33,34]

Several experimental studies to date have explored intercalation into the orthorhombic structure based upon $Na_{0.44}MnO_2$. Early work by Doeff et al.[35] achieved capacities of 160−180 mA h $g^{-1}$ in $Na_xMnO_2$ in a solid polymer electrolyte battery. Tarascon et al.[36] have demonstrated reversible cycling in the $x$ = 0.25−0.65 range of $Na_xMnO_2$. That work also found capacity reduction with increasing current, indicative of kinetic limitations to insertion. Tevar and Whitacre[37] considered cycling through a 0.6 V range using an aqueous electrolyte and obtained stable cycling for 1000 cycles with a specific capacity of 45 mA h $g^{-1}$. In each of these experimental studies the potential composition curve exhibits multiple transition processes, underlying the complexity of the insertion/deinsertion. Recently nanostructured needles[38] of $Na_{0.44}MnO_2$ have been synthesized and deliver capacities of 128 mA h $g^{-1}$ at 0.1 C with good cycling stability. Furthermore, recent work has also shown that $Na_{0.44}MnO_2$ nanowires with controllable oxygen defects[39] perform well as catalysts in the Li−$O_2$ battery system. Reversible energy storage capacities of up to 11 000 mA h $g^{-1}$ were obtained and lowered overpotentials demonstrated for oxygen evolution. Recent studies of $\alpha$-$MnO_2$ have also demonstrated a high initial capacity in excess of 280 mA h $g^{-1}$ for Mg-ion intercalation, though significant capacity fading occurred with cycling.[40,41] Due to its large 2 × 2 tunnels, $\alpha$-$MnO_2$ shows promise for Na-ion insertion for which we computationally evaluate the mechanisms in this work. By targeting the $\alpha$-$MnO_2$ polymorph it may be possible to overcome existing limitations on the kinetics and complex insertion processes for Na ions.

Lithium insertion into mixed $\beta$-$MnO_2$ and ramsdellite $MnO_2$ has previously been studied by Maphanga et al. using interatomic forcefield methods.[42] Sayle et al.[43−46] have also investigated $\beta$-$MnO_2$ using interatomic potentials to study the microstructure, nanoparticle formation, and mechanical properties using large-scale molecular dynamics methods. A recent density functional theory (DFT) study by Ling and Mizuno[47] has considered Li-ion and lithium oxide insertion into $\alpha$-$MnO_2$. That work considered structural distortions upon lithiation and the thermodynamics of insertion. They also considered the effect of $Li_2O$ insertion upon the electronic structure, a topic that we return to treat in detail. Cockayne and Li[48] have also studied magnetic and electronic structure properties with DFT. Recent work by Trahey et al.[49] has treated the thermodynamics of Li-ion and Li-oxide insertion at the surface of $\alpha$-$MnO_2$, which suggested that Li-oxide insertion and extraction may be an active mechanism in the performance of $\alpha$-$MnO_2$ as a catalyst in the Li−$O_2$ battery system.

Sodium insertion into orthorhombic $Na_{0.44}MnO_2$ has recently been studied using DFT.[50] That work analyzed the mechanism, particularly insertion sites, for the intercalation and gave comparison to experimental voltages and volume changes. But to our knowledge theoretical studies of the electrochemical Na-ion insertion into $\alpha$-$MnO_2$ are absent in the literature. Therefore, this work gives the first theoretical insights into the key mechanisms of Na-ion intercalation for $\alpha$-$MnO_2$.

Due to the renewed interest in $\alpha$-$MnO_2$, in this work we perform a comprehensive *ab initio* study of its intercalation behavior. A key question is to understand the effect of Li-ion insertion on the structure of $\alpha$-$MnO_2$. The results are organized as follows. First we outline our computational methods. Then we present results on the intercalation voltage for both Li-ion and Na-ion insertion, with a comparison to experiment. This is followed by results on the paths and energetics of ion migration. Lastly the effect of $Li_2O$ incorporation within the $\alpha$-$MnO_2$ structure is investigated. Experimental evidence demonstrates that $Li_2O$ may stabilize $\alpha$-$MnO_2$ during intercalation and is also likely to form when $\alpha$-$MnO_2$ is used as a catalyst in Li−air batteries.

## 2. METHODS

We have calculated the electronic structure using the Generalized Gradient Approximation[51] (GGA) with Hubbard U corrections (GGA +U). The incorporation of the +U corrections has been shown to improve the description of intercalation voltages via a more realistic description of the electronic structure including the band gap.[52] The VASP[53] code was employed using PAW potentials. The cutoff for the planewave basis set was 520 eV and a minimum of 6 × 6 × 6 $k$-points was used for each calculation. Where stated in the results the all electron full-potenial code Wien2k was also employed. Here $RK_{max}$ was set to 7.0 and the radii of the muffin tins was 2.01 $a_0$ for manganese, 1.51 $a_0$ for oxygen, and 1.51 $a_0$ for lithium.

The value of the $U$ parameter for our GGA+U calculations was determined *ab initio* using Wien2k.[54,55] For $\alpha$-$MnO_2$ we obtain $U$ = 5.6 eV, and after lithium intercalation we obtain $U$ = 4.8 eV for $\alpha$-$LiMnO_2$.


dx.doi.org/10.1021/cm400864n | *Chem. Mater.* 2013, 25, 2515−2526

To obtain intercalation voltages we require a single value of $U$ for both the delithiated and lithiated materials. We therefore follow the practice in previous studies[52] and use the average from the two calculations, $(U - J) = 5.2$ eV, for the spherical part of the interaction for the remainder of this study. Since the exchange interaction is poorly screened in solids[56,57] and the use of nonzero $J$ in GGA+U has recently been demonstrated[58] to be important to the description of $MnO_2$ systems, we employ an atomic limit value $J = 1.0$ eV. The same parameters are employed for the Na-ion intercalated systems due to the similarity of the valence states involved. Such DFT+U methods have been applied successfully to studies of other lithium battery materials.[52,59]

## 3. DILUTE LI-ION AND NA-ION INTERCALATION: VOLTAGE AND STRUCTURAL CHANGES

Structural optimization of the $\alpha$-$MnO_2$ crystal was performed, which adopts the tetragonal space group $I4/m$ (No. 87). In Table 1 we show the calculated lattice parameters for $\alpha$-$MnO_2$

**Table 1. Predicted GGA+U and Experimental[12] Lattice Parameters for $\alpha$-$MnO_2$**

| $\alpha$-$MnO_2$ | $a$ (Å) | $b$ (Å) | $c$ (Å) | $\alpha,\beta,\gamma$ (deg) |
|---|---|---|---|---|
| GGA+U | 9.907 | 9.907 | 2.927 | 90 |
| Experimental | 9.750 | 9.750 | 2.861 | 90 |

from GGA+U. These results agree with the experimental parameters within 2.5% and also show that the usual tendency for GGA+U to overestimate the unit cell volume is evident.

For the lithiated case, $\alpha$-$Li_xMnO_2$, the structure has not been determined fully experimentally. Consequently, we have performed a series of total energy calculations to determine the likely sites for lithium intercalation. These total energy calculations are performed with one lithium ion in a $1 \times 1 \times 2$ supercell (48 atoms) of $\alpha$-$MnO_2$. This corresponds to $\alpha$-$Li_{0.0625}MnO_2$ and is a dilute limit of intercalation. We will return to consider intercalation beyond the dilute limit.

The possible insertion sites are labeled in Figures 2 and 3. Figure 2 illustrates 4*c*, 8*h*′, and 2*a* sites from both an oblique perspective and along the *c*-axis. These three sites all lie in the same plane as the 2*a* site as indicated by the green plane perpendicular to the *c*-axis and passing through the 2*a* site. Figure 3 shows three further sites, 4*e*, 8*h*, and 2*b*. The 8*h* and 2*b* sites are coplanar, but the 4*e* site is not at a high symmetry plane lying at general coordinate (0,0,*z*). We note that formally the 8*h*′ of Figure 2 and 8*h* of Figure 3 have the same Wyckoff site symmetry, but the 8*h*′ site lies nearer to a 2*a* site, with which it is coplanar, giving it a different coordination.

The resulting energies for insertion at these sites are presented in Table 2. For lithium insertion, the position within the $2 \times 2$ tunnel adjacent to coordinating oxygen is found to be the lowest energy site. This position is nearest to an 8*h* Wyckoff position in agreement with the results of Ling and Mizuno.[47] It is important also to note that intercalation at the 8*h*′ sites lies only 24 meV higher and therefore a mixed occupation, particularly at finite temperature, may occur.

Table 2 also shows the site energies for insertion of sodium ions. On initial inspection the favored sites appear similar to those for Li-ion insertion, but the low energy sites for Na-ion insertion all lie near the center of the tunnel. This is in contrast to the Li ions that prefer to hug the tunnel wall. The Na ion lies 0.7 Å closer to the tunnel center. To illustrate the difference we show the favored site for Li-ion (Shannon radius[60] 0.76 Å) and Na-ion (Shannon radius 1.02 Å) insertion together in Figure 4.

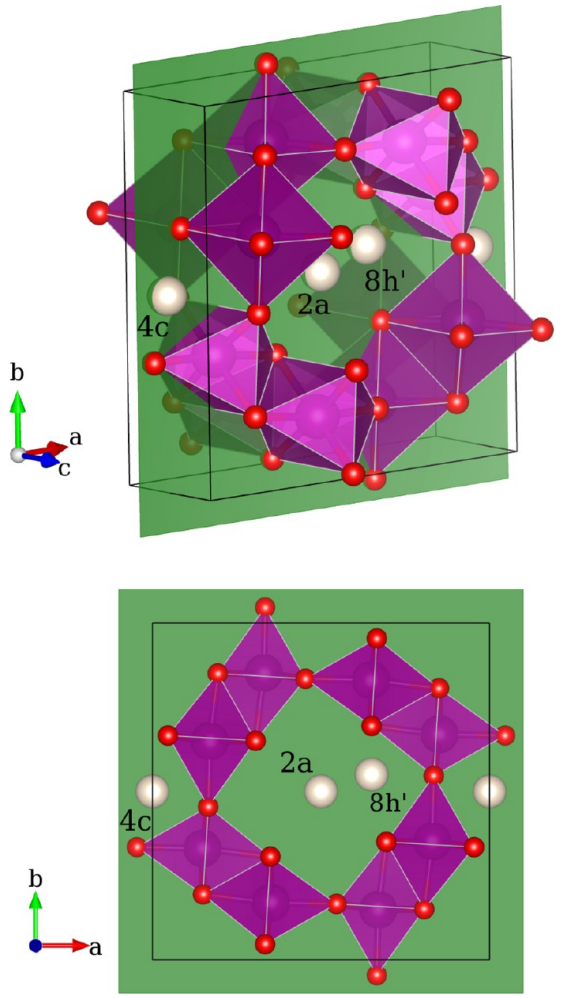


**Figure 2.** Crystal structure of $\alpha$-$MnO_2$ with insertion sites 4*c*, 8*h*′, and 2*a* labeled by the nearest Wyckoff position. The green plane perpendicular to the *c*-axis and passing through (0,0,0.5) illustrates that the three sites are coplanar. Small (red) spheres are oxygen, and large (purple) manganese lie inside the approximate $MnO_6$ octahedra.

Following sodium insertion to $\alpha$-$Na_{0.0625}MnO_2$ the obtained cell parameters are only 1% larger than for lithium at this low level of intercalation indicating that little additional stress is introduced by using sodium in place of lithium at the dilute limit.

Importantly, the energy differences between both Li-ion and Na-ion sites are small compared to the thermal energy at room temperature ($k_BT = 26$ meV). To more precisely consider the thermal energy in the system we have calculated the phonon spectrum of $\alpha$-$MnO_2$ using Phonopy.[61] The thermal contribution to the internal energy at room temperature is 82 meV per manganese. Consequently it is likely that several of the insertion sites in Table 2 are accessible from the low energy 8*h* site. We will return to discuss how the phonon energy scales compare to the formation energies at higher insertion in the $\alpha$-$Li_xMnO_2$.

The calculated intercalation voltages for the optimal insertion sites in Table 2 are determined corresponding to a comparison of end members $\alpha$-$MnO_2$ and $\alpha$-$(Li,Na)_{0.0625}MnO_2$. For Li-ion insertion we obtain 3.36 V vs $Li/Li^+$, consistent with the experimental discharge curves of Rossouw et al.[62] (≈3.5 V vs $Li/Li^+$) and Johnson et al.[12] and Kijima et al.[63] (≈3.35 V vs $Li/Li^+$). Importantly, no clear voltage plateau is found in the


dx.doi.org/10.1021/cm400864n | Chem. Mater. 2013, 25, 2515−2526

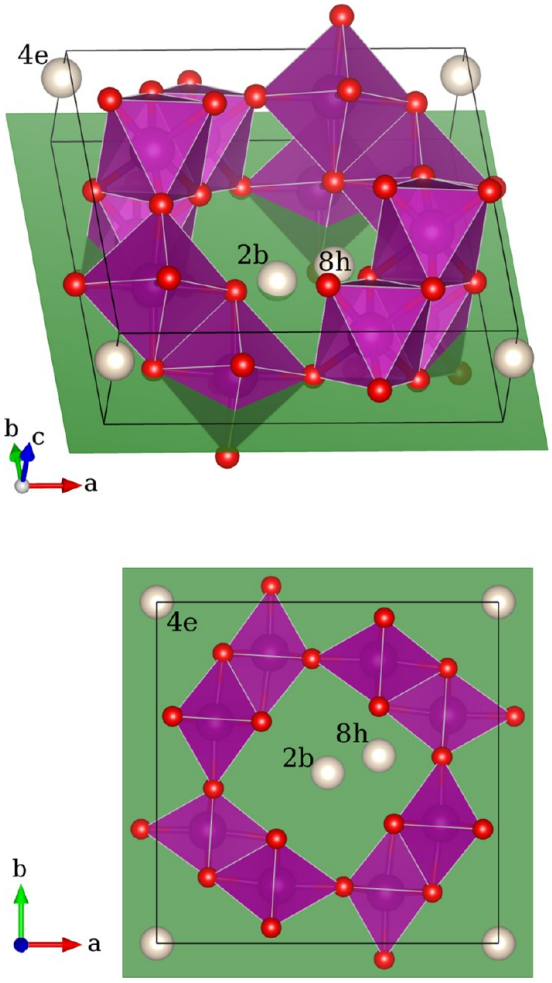


**Figure 3.** Crystal structure of $\alpha$-$MnO_2$ with insertion sites 4*e*, 8*h*, and 2*b* labeled by the nearest Wyckoff position. The green plane perpendicular to the *c*-axis and passing through (0,0,0) illustrates that the 8*h* and 2*b* sites are coplanar, but the 4*e* site is not, being at a general position (0,0,*z*). Small (red) spheres are oxygen, and large (purple) manganese lie inside the approximate $MnO_6$ octahedra.

**Table 2. Site Energies of Dilute Intercalation of $(Li,Na)^+$ Ions into $\alpha$-$MnO_2$ To Form $\alpha$-$(Li,Na)_{0.0625}MnO_2$[a]**

| ion site | $\Delta E$(Li-ion) (meV) | $\Delta E$(Na-ion) (meV) |
|---|---|---|
| 8*h* | 0 | 0 |
| 8*h*′ | 24 | 17 |
| 4*e* | 42 | 23 |
| 2*a* | 55 | 21 |
| 2*b* | 95 | 28 |
| 4*c* | 108 | 276 |

[a]Energies are given relative to a zero set for the optimal 8*h* site.

experimental discharge curves, indicating that insertion is not a two-phase process. Therefore a solid solution of lithium is expected. For Na ions a voltage of 3.23 V vs $Na/Na^+$ is predicted. Interestingly this voltage is not much lower than that for lithium which indicates that the larger size of the sodium ion does not significantly impact the thermodynamics of intercalation in the dilute limit.

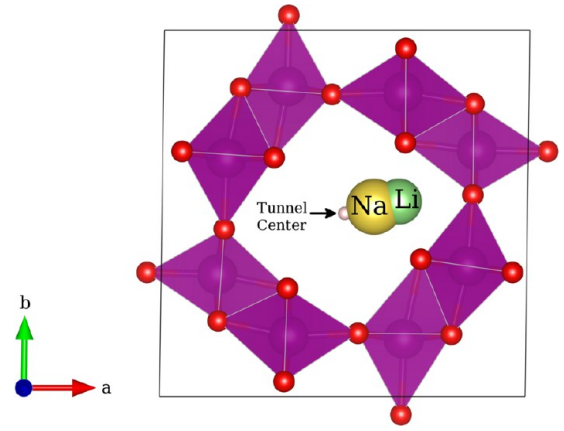


**Figure 4.** View down the *c*-axis channel of $\alpha$-$MnO_2$ with relaxed insertion sites for both Li ions and Na ions in the dilute limit. The smaller Li ion is stabilized near the tunnel wall.

## 4. LI-ION INTERCALATION OF $\alpha$-$LI_XMNO_2$: BEYOND THE DILUTE LIMIT ($X > 0.0625$)

Since the intercalation is not two-phase in $\alpha$-$MnO_2$ it is useful to consider the mechanism of intercalation at partial lithiation. Ling and Mizuno[47] have calculated the formation energy of the series $\alpha$-$Li_xMnO_2$ for $x = 0$ to $x = 1$ assuming insertion at the 8*h* site. The 8*h* site was chosen based upon calculation of the favorable insertion sites at small lithium compositions $x = 0$ to $x = 0.125$. We have extended the treatment at partial lithiation by considering insertion configurations on 8*h* and 8*h*′ sites at compositions $x > 0.125$. We separate the presentation of our results into first "Insertion Sites and Formation Energies" and secondly "Structural Distortion and Stabilization with $Li_2O$".

**4.1. Insertion Sites and Formation Energies.** Insertion at 8*h* and 8*h*′ sites was considered by calculating the total energy of all symmetry inequivalent structures using the Site-Occupation Disorder utility.[64] For compositions $0 \leq x \leq 0.5$ our results indicate that insertion at the 8*h* site has the lowest energy in agreement with Ling and Mizuno.[47] However, for compositions $0.5 < x \leq 1$ we find that the 8*h*′ site is favored. This alters the formation energies and voltages. Furthermore, it is these higher levels of insertion that are likely to be important to the structural changes that occur to $\alpha$-$MnO_2$ upon lithium insertion. Consequently, we focus on presenting results for this range of compositions. In Table 3 the site energies for Li-ion intercalation are shown for compositions $0.5 \leq x \leq 1$. For $\alpha$-

**Table 3. Relative Site Energy per Li Ion for Insertion at the 8*h*′ Compared to the 8*h* Site and the Formation Energy of the Lowest Insertion Configuration for Compositions Containing Increasing Quantities of Lithium[a]**

| composition | $\Delta E(8h'-8h)$ (meV) | $E_{Formation}$ (meV/Mn) |
|---|---|---|
| $\alpha$-$Li_{0.5}MnO_2$ | 317 | 0.0 |
| $\alpha$-$Li_{0.625}MnO_2$ | −1 | 145.4 |
| $\alpha$-$Li_{0.75}MnO_2$ | −214 | 31.2 |
| $\alpha$-$Li_{0.875}MnO_2$ | −20 | 129.7 |
| $\alpha$-$LiMnO_2$ | −53 | 0.0 |

[a]The zero reference for the site energies is taken as the energy for the 8*h* site; therefore, negative values indicate the 8*h*′ site is more stable while positive values show the 8*h* site is more stable. Formation energies are calculated from the lowest energy structure at each composition using eq 1.


dx.doi.org/10.1021/cm400864n | *Chem. Mater.* 2013, 25, 2515−2526

$Li_{0.5}MnO_2$ the 8*h* site is strongly favored, consistent with our dilute-limit results and those of Ling and Mizuno.[47] However, as further lithium is inserted, the 8*h*′ site becomes more favorable, essentially degenerate with 8*h* for $\alpha$-$Li_{0.625}MnO_2$, and then strongly favored by 214 meV per Li-ion for $\alpha$-$Li_{0.75}MnO_2$. The 8*h*′ site remains favored for both $\alpha$-$Li_{0.875}MnO_2$ and fully lithiated $\alpha$-$LiMnO_2$.

It is also important to assess whether the formation of these compositions is thermodynamically stable. The formation energies for the low energy structures in the range $0.5 \leq x \leq 1$ are also shown in Table 3. The formation energy was calculated with respect to the end points $\alpha$-$Li_{0.5}MnO_2$ and $\alpha$-$LiMnO_2$ with the expression

$$E_F = E_x - (2x - 1) \times E(\alpha\text{-}Li_{0.5}MnO_2) - (2 - 2x) \times E(\alpha\text{-}LiMnO_2) \quad (1)$$

Lithium insertion at $\alpha$-$Li_{0.75}MnO_2$, corresponding to six lithium ions on 8*h*′ sites in the unit cell, gives a positive formation energy of only 31 meV per manganese. Therefore, based on the zero temperature DFT energy, this composition will lie just above the convex hull. Yet, the small energy of 31 meV is comparable to the thermal energy scale at room temperature and consequently may be accessible at battery operating temperatures. To quantify the thermal energy in the system the phonon spectrum of $\alpha$-$LiMnO_2$ has been calculated. We find that, at room temperature, the phonon vibrational contributions to the internal energy are 123 meV per manganese. This strongly suggests that the $\alpha$-$Li_{0.75}MnO_2$ composition will be thermodynamically accessible during cycling at room temperature. However, the other intermediate compositions $x = 0.625$ and $x = 0.875$, with formation energies of 145.4 and 129.7 meV/Mn, respectively, are unlikely.

The lowest energy structures of $\alpha$-$Li_xMnO_2$ for important compositions ($x = 0.25$, $x = 0.5$, $x = 0.75$, and $x = 1.0$) are shown in Figure 5 and indicate that lithium ions distribute themselves as uniformly as possible to minimize the Li−Li Coulomb repulsion. This can be observed from the fact that the low energy structure in Figure 5b of $\alpha$-$Li_{0.5}MnO_2$ contains two Li ions in each 2 × 2 tunnel. In Figure 5c, the structure of $\alpha$-$Li_{0.75}MnO_2$ contains three Li ions in each 2 × 2 tunnel. Other combinations where four or more Li ions lie in a single tunnel are considered in the 31 distinct structures, but all lie significantly higher in energy.

The displacement of the intercalated lithium ions from 8*h* to 8*h*′ sites as lithiation proceeds is driven by the need to reduce the mutual Coulomb repulsion of the lithium ions once a higher concentration level is placed within the open tunnel. To demonstrate why occupation of the 8*h*′ site is better at reducing the energy penalty, layer separated structures are useful. In Figure 6 the structure of $\alpha$-$LiMnO_2$ is shown with lithium intercalated at the 8*h*′ and 8*h* sites. The Li ions at 8*h*′ sites reside in a plane and alternate in a ring with oxygen sites, which is particularly evident for the yellow plane in Figure 6b. In contrast, for the Li-ions residing at 8*h* sites it is clear that there are no oxygen ions alternating between the lithium positions in order to reduce the Li-ion to Li-ion Coulomb repulsion. Consequently, while in the dilute limit the strong coordination of the 8*h* site with the oxygen wall and the larger cavity space made it more favorable, the lack of in-plane oxygens to reduce the Coulomb repulsion between Li-ions means that at higher intercalation levels the 8*h*′ site becomes more energetically favorable.

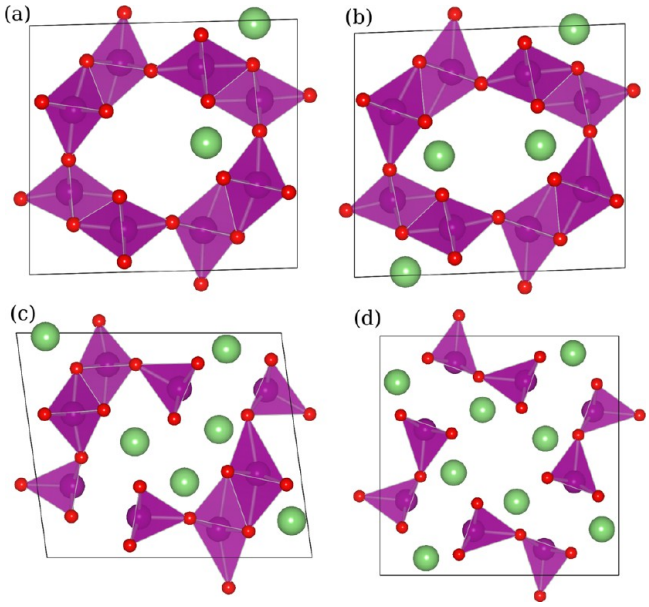


**Figure 5.** Lowest energy structures obtained for the unit cell of (a) $\alpha$-$Li_{0.25}MnO_2$, (b) $\alpha$-$Li_{0.5}MnO_2$, (c) $\alpha$-$Li_{0.75}MnO_2$, and (d) $\alpha$-$Li_1MnO_2$. The polyhedra are connected by Mn−O bonds of length 2.7 Å. Red spheres are oxygen, purple is manganese, and green spheres are lithium.

### 4.2. Structural Distortion and Stabilization with $Li_2O$.

The importance of the thermodynamically accessible $\alpha$-$Li_{0.75}MnO_2$ composition to the cyclability becomes even more evident upon inspection of the optimized structure as shown in Figure 5c. The structure is clearly strongly distorted due to the lithium insertion. The distortion results in a ratio $a/b = 1.21$ of the in-plane lattice parameters and an of angle 97.1° between their respective vectors (Table 4). Second, the octahedral coordination of the Mn ions is broken, particularly at edge-sharing links. It appears that the associated oxygens instead coordinate with the Li ions preferentially to Mn ions. These distortions are larger than those that we find at other compositions. At other accessible compositions the deviation of the cell angle from 90° is always less than 2° and $a/b < 1.21$. Together this means that at other compositions the distortion to the octahedra is smaller.

From Figure 5d it is clear that the unit cell expansion of $\alpha$-$LiMnO_2$ stretches the octahedra significantly. The unit cell volume expands by 30% compared to delithiated $\alpha$-$MnO_2$. Given that experimentally the lithium intercalation capacity of $\alpha$-$MnO_2$ has been found to reach 240 mA h $g^{-1}$[13,62] (corresponding to $\alpha$-$Li_{0.78}MnO_2$) it is clear that intercalation must proceed beyond $x = 0.5$. Furthermore, the structures of $\alpha$-$Li_{0.25}MnO_2$ and $\alpha$-$Li_{0.5}MnO_2$ shown in Figure 5a,b, although having asymmetric *a* and *b* lattice parameters, possess comparatively little distortion to the $MnO_6$ octahedra. Consequently it is argued that the degradation of the structure of $\alpha$-$MnO_2$ with cycling is driven by distortions to the $MnO_6$ octahedra at lithiation levels $0.5 < x \leq 1$. Ling and Mizuno[47] also highlighted the importance of the Jahn−Teller driven anisotropic expansion of the cell in the range $0.25 < x \leq 0.5$ that results in a significantly larger *a*-axis than *b*-axis, $a/b = 1.19$ for $\alpha$-$Li_{0.5}MnO_2$.

The relaxed structure of $\alpha$-$LiMnO_2$ with ions at the 8*h*′ sites shows greater distortion in unit cell angles and ratio of cell parameters $a/b$ compared to the structure with Li-ions at 8*h*


dx.doi.org/10.1021/cm400864n | Chem. Mater. 2013, 25, 2515−2526

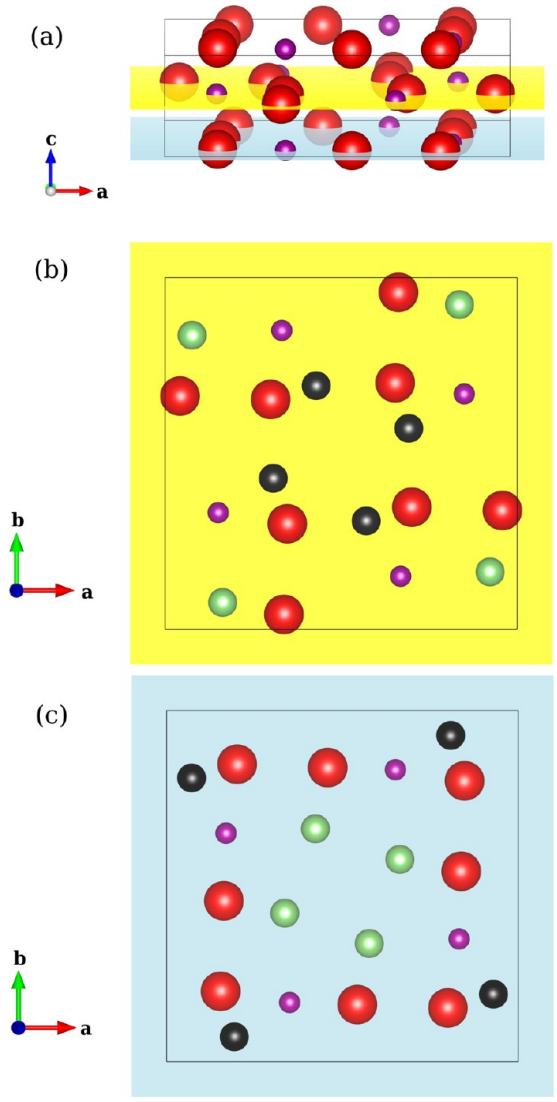


**Figure 6.** Layer separated structure of $\alpha$-$LiMnO_2$ with lithium occupying the 8$h'$ sites (black spheres) and 8$h$ sites (green spheres). Depicted in (a) is pristine $\alpha$-$MnO_2$ from an oblique view, in (b) the layer passing through (0,0,0.5) with 8$h$ and 8$h'$ sites, and in (c) the layer passing through (0,0,0) with 8$h$ and 8$h'$ sites. The 8$h$ sites occupy a larger cavity space, but the 8$h'$ sites reside in rings that alternate with oxygen. Red spheres are oxygen and purple manganese.

**Table 4. Selected Cell Parameters for Compositions Containing the Same Quantity (No.(Li)/No.(Mn) = 0.75) of Li Ions $\alpha$-$Li_{0.75}MnO_2$ and $\alpha$-0.125$Li_2O$·$Li_{0.5}MnO_2$ with a Stabilizing Oxygen at the 2$a$ site[a]**

| composition | insertion site | $a/b$ | $\gamma$ (deg) |
|---|---|---|---|
| $\alpha$-$MnO_2$ | - | 1 | 90 |
| $\alpha$-$Li_{0.75}MnO_2$ | 8$h'$ | 1.21 | 97.1 |
| $\alpha$-$Li_{0.75}MnO_2$ | 8$h$ | 1.10 | 94.0 |
| $\alpha$-0.125$Li_2O$·$Li_{0.5}MnO_2$ | 8$h$ | 1.12 | 96.6 |

[a] $\alpha$-$MnO_2$ is included to aid the comparison.

sites. As shown in Table 4, moving from 8$h$ to 8$h'$ sites increases the cell angle distortion from $\gamma$ = 94.0° to $\gamma$ = 97.1°. The distortion of the cell parameters increases from $a/b$ = 1.10 to $a/b$ = 1.21. The relaxed structure of $\alpha$-$LiMnO_2$ with ions at the 8$h'$ sites possesses a unit cell volume that is 7% greater than that if it remained on the 8$h$ site. This is largely due to significant distortion of the $MnO_6$ octahedra as the Li ions attempt to maximize their oxygen ion coordination. This result demonstrates that it is in fact energetically favorable for the structure to be more distorted at higher levels of lithiation. The movement of ions from the 8$h$ to 8$h'$ sites as intercalation increases may also be kinetically slow. The required ionic migrations may distort the structures further.

Experimental investigations on pure $\alpha$-$MnO_2$ have demonstrated a lithium intercalation capacity of 240 mA h $g^{-1}$ (≈ 0.7 Li per Mn).[62] However, upon cylcing this capacity degrades. This instability is attributed experimentally[7,13] to the absence of stabilizing cations in the large 2 × 2 structure that forms the basis of $\alpha$-$MnO_2$. The large structural distortions predicted by our calculations for $\alpha$-$Li_{0.75}MnO_2$ and volume expansion for $\alpha$-$LiMnO_2$ indicate a mechanism via which the structure destabilizes. Further experimental treatment by insertion of stabilizing $Li_2O$ with small quantities of ammonia results in good cycling stability. Johnson and Thackeray have observed[13] a stable capacity of 220 mA h $g^{-1}$ for ammonia treated $\alpha$-[0.143$Li_2O$]-$MnO_2$.

To examine the effect of $Li_2O$ on the structural stability of lithiated $\alpha$-$MnO_2$ a unit cell of $\alpha$-0.125$Li_2O$·$Li_{0.5}MnO_2$, which has an additional oxygen atom at the center of a 2 × 2 tunnel relative to $\alpha$-$Li_{0.75}MnO_2$, was considered. This structure contains exactly the same number of lithium atoms as $\alpha$-$Li_{0.75}MnO_2$ and therefore a comparison with this structure allows us to probe the effect of the additional oxygen. The optimized structure obtained is shown in Figure 7b, alongside

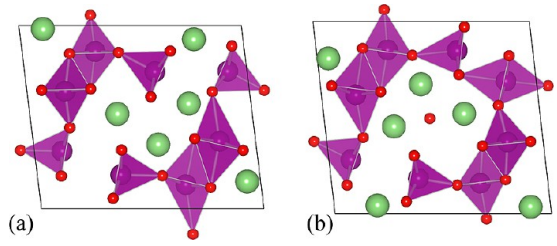


**Figure 7.** Comparison of the lowest energy structures obtained for compositions containing the same quantity (No.(Li)/No.(Mn) = 0.75) of Li ions (a) $\alpha$-$Li_{0.75}MnO_2$ and (b) $\alpha$-0.125$Li_2O$·$Li_{0.5}MnO_2$ with a stabilizing oxygen at the 2$a$ site. The polyhedra are connected by Mn−O bonds of length 2.7 Å.

$\alpha$-$Li_{0.75}MnO_2$ in Figure 7a, and is significantly less distorted than that obtained without the additional oxygen. The ratio of the in-plane lattice vectors is $a/b$ = 1.12, and there is an angle 96.6° between them. Viewed alongside the result in the absence of the stabilizing oxygen in Table 4, it is clear that the incorporation of $Li_2O$ reduces the structural distortion significantly. Furthermore, it is clear from comparing Figure 7a,b that the degree to which the edge-sharing links are broken is reduced. The reduction in distortion can be attributed to the presence of the additional oxygen anion at the center of the 2 × 2 tunnel which provides stable coordination for the lithium ions that consquently reduces distorting interactions with the surrounding $MnO_6$ octahedra. We also find that the incorporation of $Li_2O$ fundamentally alters the electronic structure, a topic we will return to.

The incorporation of $Li_2O$ at the higher level of lithiation, $\alpha$-$LiMnO_2$, has also been treated. Relaxed structures were obtained for $\alpha$-0.125$Li_2O$·$Li_{0.75}MnO_2$ and $\alpha$-


dx.doi.org/10.1021/cm400864n | Chem. Mater. 2013, 25, 2515−2526

$0.25Li_2O{\cdot}Li_{0.5}MnO_2$. The key result is presented in Table 5 where the volume of the unit cell is found to decrease with

**Table 5. Predicted Unit Cell Volumes for Fully Lithiated $\alpha$-$LiMnO_2$ and with Increasing Stabilizing Oxygen To Form $\alpha$-$0.125Li_2O{\cdot}Li_{0.75}MnO_2$ and $\alpha$-$0.25Li_2O{\cdot}Li_{0.5}MnO_2$[a]**

| composition | volume (Å$^3$) | $\Delta V$ (%) |
|---|---|---|
| $\alpha$-$MnO_2$ | 287.3 | 0.0 |
| $\alpha$-$LiMnO_2$ | 374.3 | 30.3 |
| $\alpha$-$0.125Li_2O{\cdot}Li_{0.75}MnO_2$ | 355.7 | 23.8 |
| $\alpha$-$0.25Li_2O{\cdot}Li_{0.5}MnO_2$ | 347.8 | 21.1 |

[a]The percentage volume expansion relative to $\alpha$-$MnO_2$ is also quoted. The corresponding unit cells are depicted in Figure 8.

increasing content of the stabilizing oxygen. This is likely a result of having additional negative $O^{2-}$ ions that act to reduce the mutual repulsion of the lithium ions. The resulting relaxed structures are shown in Figure 8 where it is clear that, with the

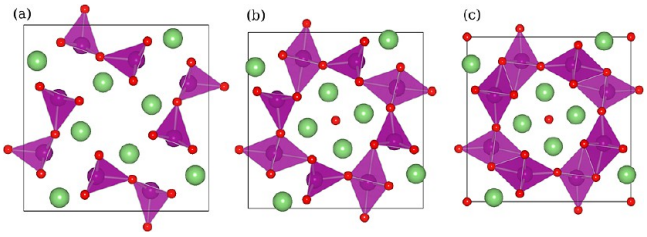


**Figure 8.** Comparison of the lowest energy structures obtained for compositions containing the same quantity (No.(Li)/No.(Mn) = 1) of Li ions (a) $\alpha$-$LiMnO_2$ and with increasing stabilizing oxygen to form (b) $\alpha$-$0.125Li_2O{\cdot}Li_{0.75}MnO_2$ and (c) $\alpha$-$0.25Li_2O{\cdot}Li_{0.5}MnO_2$. Mn−O bonds of length 2.7 Å.

smaller unit cell volume, the $MnO_6$ octahedra better maintain their structural integrity in the presence of the stabilizing oxygen. This is likely to be a key factor in the improved structural stability of $Li_2O$ treated $\alpha$-$MnO_2$ when cycled as an intercalation cathode.

## 5. NA-ION INTERCALATION $\alpha$-$NA_XMNO_2$: BEYOND THE DILUTE LIMIT ($X$ > 0.0625)

Due to the large tunnel structures in $\alpha$-$MnO_2$ it is viewed as a viable candidate material for a sodium intercalation cathode. The significant cost advantages of Na-ion batteries offer the potential to extend the use of such batteries to important new applications such as smart energy grids and renewable energy storage. Atomistic first-principles methods offer a valuable way to obtain insight into hitherto unexplored candidate materials for Na-ion intercalation electrodes. In this section we consider the structure and thermodynamic stability of Na-ion intercalated $\alpha$-$Na_xMnO_2$.

**5.1. Insertion Sites and Formation Energies.** To probe the insertion sites and thermodynamic stability of the intercalated system $\alpha$-$Na_xMnO_2$, we use the convex hull method.[65] Key to this is calculation of the energy of formation of $\alpha$-$Na_xMnO_2$ for $0 < x < 1$. For each value of $x$ all symmetry inequivalent structures were considered using the Site-Occupation Disorder utility.[64] As with Li-ions, in the previous section, insertion at $8h$ and $8h'$ sites was considered. The formation energies were calculated with respect to the end members $\alpha$-$MnO_2$ and $\alpha$-$NaMnO_2$ with the formula:

$$E_F = E_x - xE(\alpha\text{-}NaMnO_2) - (1-x)E(\alpha\text{-}MnO_2) \quad (2)$$

The formation energies and convex hull are presented in Figure 9 and indicate that the insertion process is multistage. This is

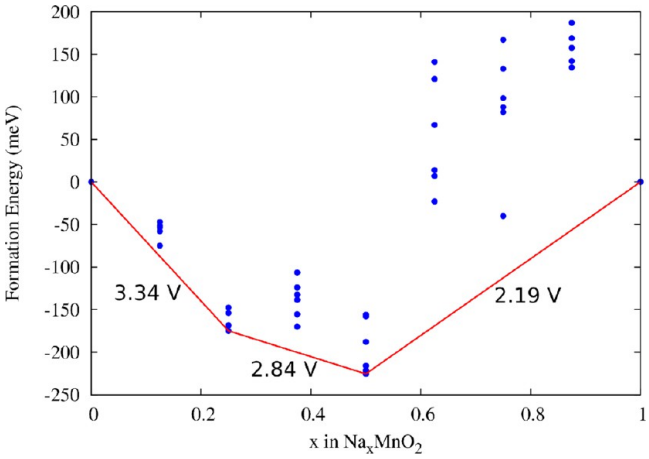


**Figure 9.** Formation energies and convex hull of $\alpha$-$Na_xMnO_2$ for $0 < x < 1$. The obtained voltages for steps along the convex hull are also indicated.

consistent with experimental work on sodium insertion in other $MnO_2$ materials.[35,36] The thermodynamically stable compositions from this curve lie at $x = 0$, $x = 0.25$, $x = 0.5$, and $x = 1$. The convex hull based on GGA+U energies exhibits three insertion steps, each step delivering a lower voltage as the intercalation level is increased. The obtained voltages are 3.34 V followed by 2.84 V and then 2.19 V in the final step. These voltages are approximately 0.15 V lower than those obtained for Li-ion insertion.[47] This is likely a consequence of greater energy penalty in accommodating the larger sodium ion. It is also of interest to note that for the three thermodynamically stable levels of intercalation ($x = 0.25$, 0.5, and 1) it is the $8h$ site that is the stable insertion site.

For the composition $\alpha$-$Na_{0.75}MnO_2$ the lowest energy structure prefers occupation of the $8h'$ site. For Na ions and Li ions the $8h'$ is favored at $x = 0.75$, but for Na ions the preferred site shifts back to $8h$ at $x = 1$ which is not the case for Li ions. Consequently, it is clear that Na-ion intercalation shows a differing trend than that of Li ions with respect to preferred intercalation site. The lowest energy structure at $x = 0.75$ for Na-ion intercalation lies 75 meV above the convex hull, which is still accessible thermodynamically given that the thermal energy is approximately 123 meV per manganese ion. However, this structure is likely to play a smaller role than for the case of Li-ion intercalation where we found the $x = 0.75$ composition lay just 31 meV above the convex hull. The composition $x = 0.125$ is just 4 meV above the convex hull and therefore well within the accessible range of thermal energy vibrations. Similarly $x = 0.375$ is 26 meV above the convex hull and is also likely to be present at battery operating temperatures.

**5.2. Structural Distortion and Stabilization with $Na_2O$.** The lowest energy structures of $\alpha$-$Na_xMnO_2$ for $x = 0.25$, 0.5, and 1 are shown in Figure 10. It is clear that even at $x = 0.5$ the structure of the unit cell is significantly distorted, where the cell parameters distort to $a/b = 1.28$ and the angle $\gamma = 98°$ (Table 6). At the same level of Li-ion intercalation the cell angle deviated by less than 2° from $\gamma = 90°$. This underlines the


dx.doi.org/10.1021/cm400864n | Chem. Mater. 2013, 25, 2515−2526

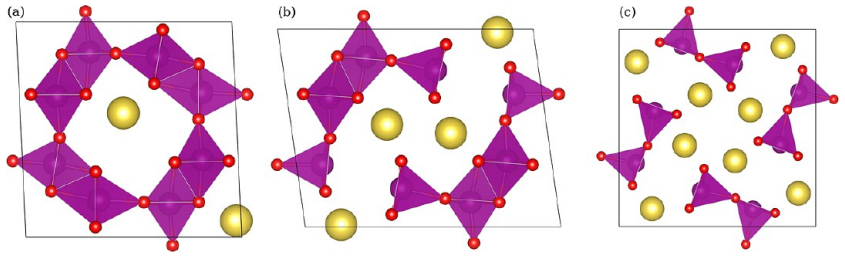


**Figure 10.** Lowest energy structures of $\alpha$-$Na_xMnO_2$ for (a) $x = 0.25$, (b) $x = 0.5$, and (c) $x = 1$.

**Table 6. Predicted Lattice Parameters for Sodium Intercalated $\alpha$-$MnO_2$**

| composition | $a$ (Å) | $b$ (Å) | $c$ (Å) | $a/b$ | $\gamma$ (deg) |
|---|---|---|---|---|---|
| $\alpha$-$MnO_2$ | 9.907 | 9.907 | 2.861 | 1 | 90.0 |
| $\alpha$-$Na_{0.25}MnO_2$ | 10.06 | 10.01 | 2.94 | 1.01 | 92.6 |
| $\alpha$-$Na_{0.5}MnO_2$ | 12.06 | 9.43 | 2.89 | 1.28 | 98.0 |
| $\alpha$-$NaMnO_2$ | 12.133 | 12.133 | 2.863 | 1 | 90.0 |

additional challenge in accommodating the larger Na ion. The effect of Jahn–Teller distortion is likely to be active in producing the large $a/b$ ratio, but other effects are also active as indicated by the large distortion in $\gamma$. Important lattice parameters for these structures are summarized in Table 6. Due to the larger size of the Na ion, the effects of mutual repulsion between ions begin to distort the structure when there are fewer Na ions in the tunnel, i.e., lower intercalation levels. This suggests that the use of cycling in restricted ranges in recent work[37,38] has in part achieved stable cycling by avoiding structural degradation.

The enhanced impact of the Na-ion size is also evident from the predicted cell volume of 420.8 Å$^3$ for $\alpha$-$NaMnO_2$ compared to 374.3 Å$^3$ when Li-ions are intercalated. Conseqently we expect that, in the absence of stabilizing anions, the structural degradation of $\alpha$-$MnO_2$ with sodium intercalation will be at least as great as that for lithium.

The use of stabilizing anions could be effective for the Na-ion intercalated compound as has been demonstrated for the lithium intercalate.[13] To assess the effectiveness of $Na_2O$ species in reducing structural distortion, structural relaxation was performed for the fully intercalated $\alpha$-$NaMnO_2$ with additional stabilizing oxygens to form $\alpha$-$0.125Na_2O{\cdot}Na_{0.75}MnO_2$ and $\alpha$-$0.25Na_2O{\cdot}Na_{0.5}MnO_2$. The resulting predicted cell volumes are shown in Table 7. They indicate that the trend is the opposite to that observed for the Li-ion materials. In fact the presence of the additional oxygen species expands the volume and will therefore distort the structure of the $MnO_6$ octahedra further. Therefore, it is unlikely that the incorporation of $Na_2O$ will be effective in stabilizing the structure during Na-ion intercalation cycles.

**Table 7. Predicted Cell Volumes for Compositions Containing the Same Quantity (No.(Na)/No.(Mn) = 0.75) of Na Ions[a]**

| structure | volume (Å$^3$) | $\Delta V$ (%) |
|---|---|---|
| $\alpha$-$MnO_2$ | 287.3 | 0.0 |
| $\alpha$-$NaMnO_2$ | 421.5 | 46.7 |
| $\alpha$-$0.125Na_2O{\cdot}Na_{0.75}MnO_2$ | 428.5 | 49.1 |
| $\alpha$-$0.25Na_2O{\cdot}Na_{0.5}MnO_2$ | 431.8 | 50.3 |

[a]First is $\alpha$-$NaMnO_2$ and then $\alpha$-$0.125Na_2O{\cdot}Na_{0.75}MnO_2$ with a stabilizing oxygen at the 2a site. Finally is $\alpha$-$0.25Na_2O{\cdot}Na_{0.5}MnO_2$ with two stabilizing oxygens at the 2a sites. $\alpha$-$MnO_2$ is included to aid the comparison.

Finally, we note that the importance of mutual Coulomb repulsion between intercalated ions to the structural stability of $\alpha$-$MnO_2$ may be important to other manganese oxides with wide tunnels such as todorokite. Our results suggest that upon $Li^+$ insertion this repulsion both causes the transfer of the stable insertion site from 8*h* to 8*h*′ with increasing lithiation and is an important factor in the ability of $Li_2O$ to stabilize the structure of $\alpha$-$Li_xMnO_2$ by the additional presence of $O^{2-}$ at the tunnel center. In contrast when $Na^+$ is inserted into $\alpha$-$MnO_2$, the larger $Na^+$ ionic radius means that the incorporation of $Na_2O$ is not effective in reducing the repulsion. This may have a role in the stable cycling observed in $Na_{0.44}MnO_2$[37] due to its narrower tunnels providing better coordination of $Na^+$ to the $O^{2-}$ of the tunnel wall.

## 6. LI-ION AND NA-ION MIGRATION

Simulation methods may enhance our understanding of the ion mobility in battery cathodes by evaluating the activation energies for specific mechanisms at the atomic level. These activation energies are of considerable interest when considering the charge/discharge rates achievable by the materials. In $\alpha$-$MnO_2$ the structure possesses large 2 × 2 tunnels that are likely to dominate the lithium migration. It is desirable to consider ion migration in both the dilute limit and at more advanced stages of intercalation. For the latter we choose to consider migration in $\alpha$-$(Li,Na)_{0.75}MnO_2$ as a representative composition to indicate how increasing amounts of intercalated ions impact the migration energetics during battery operation.

Using the nudged elastic band method in 2 × 2 × 4 supercells the Li-ion migration barriers for the paths shown in Figure 11a,b were first evaluated in the dilute limit. In Figure 11a, path A is migration from 2*a* to 8*h*. Path B is migration along the *c*-axis from one 2*a* site to the next. In Figure 11b path C is migration along the *c*-axis from 8*h* to the next 8*h* site and path D is migration from one 8*h* site to another 8*h* site in-plane. The curved line in Figure 11b indicates the curved route that avoids the higher energy 2*a* site for Li ions.

The resulting Li-ion migration barriers are shown in Table 8. All paths in the dilute limit, uppermost in the table, give low barriers <0.3 eV with migration between adjacent 8*h* sites in-plane being the most favorable. The facile diffusion of ions at these low concentrations may aid the reaction kinetics when $\alpha$-$MnO_2$ is used as an electrocatalyst in the Li–$O_2$ battery system. They are also consistent with the rapid diffusion found by calculations of Trahey et al.[49]

Before considering the ion migration in systems beyond the dilute limit we first determine the most favorable insertion site for (Li,Na) ions into $\alpha$-$(Li,Na)_{0.75}MnO_2$ in a 1 × 1 × 2


dx.doi.org/10.1021/cm400864n | *Chem. Mater.* 2013, 25, 2515–2526

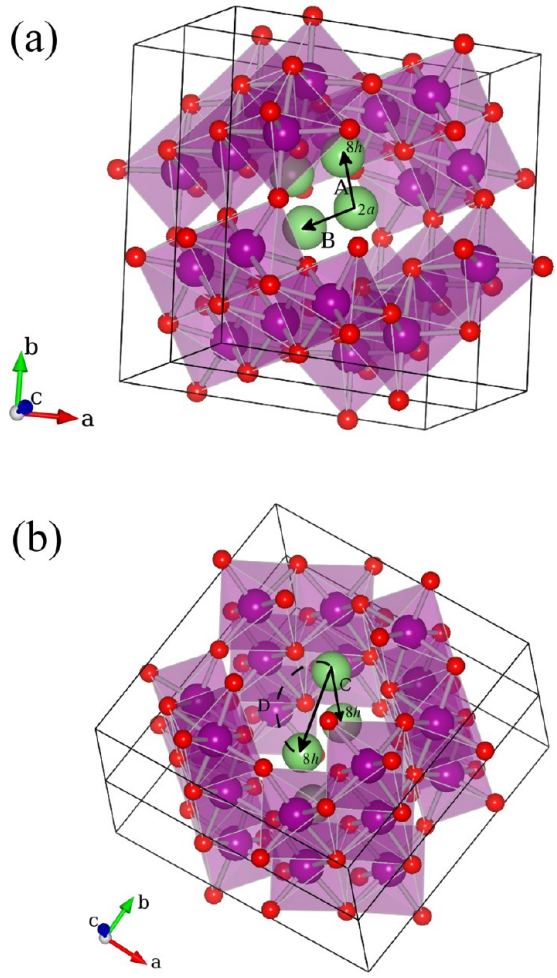


**Figure 11.** Ion migration paths of $\alpha$-$MnO_2$ involving 2*a* and 8*h* sites.

**Table 8. Energy Barriers for Lithium Migration Paths in $\alpha$-$MnO_2$ and $\alpha$-$Li_{0.75}MnO_2$**

| path | description | $\Delta E$ (eV) | distance (Å) |
|---|---|---|---|
| | $\alpha$-$MnO_2$ | | |
| A | 2*a* to 8*h* | 0.23 | 1.14 |
| B | 2*a* to 2*a* ∥ *c*-axis | 0.28 | 2.93 |
| C | 8*h* to 8*h* ∥ *c*-axis | 0.10 | 2.93 |
| D | 8*h* to 8*h* in-plane | 0.05 | 2.26 |
| | $\alpha$-$Li_{0.75}MnO_2$ | | |
| E | 8*h*′ to 8*h*′ ∥ *c*-axis | 0.55 | 2.89 |

supercell. The site energies are displayed in Table 9. For Li-ion insertion the 8*h*′ site in the same plane as the ions already present in the low energy configuration is the most favorable. An interstitial site between the Li-ion layers near 8*h* is higher by 550 meV. In contrast to the dilute limit the 2*a* site becomes highly unfavorable due to Coulombic interactions with surrounding Li ions.

**Table 9. Site Energies of Intercalation of $(Li,Na)^+$ Ions into $\alpha$-$(Li,Na)_{0.75}MnO_2$[a]**

| ion site | $\Delta E$(Li-ion) (meV) | $\Delta E$(Na-ion) (meV) |
|---|---|---|
| intercalated layer (8*h*′) site | 0 | 0 |
| center 2 × 2 tunnel (2*a*) | 1340 | 2480 |
| interstitial layer (8*h*) site | 550 | 480 |

[a]Insertion energies are given relative to a zero set for the 8*h*′ site.

The energies of the insertion sites for sodium into $\alpha$-$Na_{0.75}MnO_2$ are also listed in Table 9. The 8*h*′ site in the same plane as the Na ions already present is most favorable with the 2*a* site being less favorable still than it was for Li ions.

Since the 8*h*′ site is clearly the most favorable in Li-ion intercalated $\alpha$-$Li_{0.75}MnO_2$ the migration barrier between these sites (path E) was also determined as 0.55 eV. This value indicates a significant increase in the kinetic barriers to migration as lithiation is increased. A migration activation energy of 0.55 eV is comparable with experimental and calculated results found for other $MnO_2$ structures[66] and other operating cathode materials such as $LiFePO_4$.[67] We note that our recent DFT study has considered surface effects of Li-ion migration in rutile $\beta$-$MnO_2$.[68]

Sodium migration barriers in the dilute limit ($\alpha$-$MnO_2$) and in $\alpha$-$Na_{0.75}MnO_2$ are presented in Table 10. In the dilute limit all barriers are less than 0.14 eV. For $\alpha$-$Na_{0.75}MnO_2$ the energy activation barrier for migration between the strongly favored 8*h*′ site is 0.48 eV, which is significantly larger than the result for the dilute limit. Interestingly the migration barriers for both Li ions and Na ions are comparable, indicating that ionic radius may in some cases not be the dominant factor in determining ion diffusion.

**Table 10. Energy Barriers for Sodium Migration Paths in $\alpha$-$MnO_2$ and $\alpha$-$Na_{0.75}MnO_2$**

| path | description | $\Delta E$ (eV) | distance (Å) |
|---|---|---|---|
| | $\alpha$-$MnO_2$ | | |
| A | 2*a* to 8*h* | 0.14 | 0.82 |
| B | 2*a* to 2*a* ∥ *c*-axis | 0.09 | 2.97 |
| C | 8*h* to 8*h* ∥ *c*-axis | 0.10 | 2.97 |
| D | 8*h* to 8*h* in-plane | 0.08 | 1.64 |
| | $\alpha$-$Na_{0.75}MnO_2$ | | |
| E | 8*h*′ to 8*h*′ ∥ *c*-axis | 0.48 | 2.91 |

These results show that migration barriers in $\alpha$-$MnO_2$ increase significantly with increasing intercalation of both lithium and sodium, indicating the importance of considering Li−Li and Na−Na interactions. The favored pathways suggest that Li-ion and Na-ion diffusion in $\alpha$-$MnO_2$ is primarily one-dimensional along the 2 × 2 tunnels indicating highly anisotropic transport behavior.

## 7. $Li_2O$ INCORPORATION: ELECTRONIC STRUCTURE

Experimental investigations into $\alpha$-$MnO_2$ have found that the stability of intercalation is improved significantly with the incorporation of $Li_2O$ within the tunnel structure. The first principles methods employed in our work also allow us to inspect the effect of the presence of $Li_2O$ on the electronic structure of the system. Figure 12a shows the unit cell of $\alpha$-$0.125Li_2O{\cdot}MnO_2$ where the $Li_2O$ resides at the center of the 2 × 2 tunnel as indicated by experimental studies.[12] In Figure 12b we show the resulting density of states (DOS) for $\alpha$-$0.125Li_2O{\cdot}MnO_2$ calculated with GGA+U using 2000 *k*-points. Importantly, and in agreement with the results of Ling and Mizuno,[47] the system possesses metallic states that cross the Fermi level. However, Ling and Mizuno obtained a half-metal, while our results indicate a full metal with conducting states crossing the Fermi level in both spin channels. Our analysis shows that the likely reason why Ling and Mizuno only


dx.doi.org/10.1021/cm400864n | Chem. Mater. 2013, 25, 2515−2526

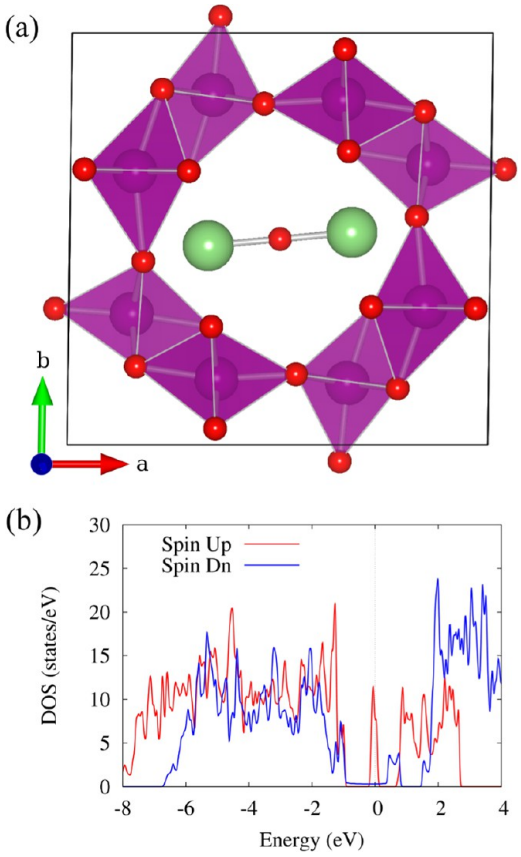


**Figure 12.** $\alpha$-0.125$Li_2O$·$MnO_2$ (a) structural unit cell and (b) density of states.

observed a half-metal was the use of too few *k*-points. In the treatment of metals, with which the present authors have extensive experience,[69−71] many more *k*-points are typically required to obtain converged results. Our testing shows that with a 6 × 6 × 6 *k*-point grid a half-metal is obtained, but a converged density of states requires at least 10 × 10 × 10 *k*-points. Increasing the quantity of $Li_2O$ further to $\alpha$-0.25$Li_2O$·$MnO_2$ has also been considered and similarly results in metallic behavior.

From an inspection of the partial density of states most of the metallic states are associated with oxygen atoms within the 2 × 2 tunnel. Since GGA+U only improves the treatment of exchange around the manganese sites we have also calculated the electronic structure with hybrid HSE06 which incorporates improved treatment of exchange for all states including the oxygen. We find that the presence of the metallic states is robust to this treatment.

In Figure 13a,b, we show the Fermi surface for the metallic states from our GGA+U calculation for spin up and down, respectively. The large amount of curvature in the spin up Fermi surface indicates that transport for spin up electrons is largely isotropic. In contrast the spin down Fermi surface is effectively two flat sheets intercepting the $k_z$ axis. Since the Fermi velocity is directed normal to the Fermi surface these flat sheets correspond to one-dimensional conduction for spin down electrons along the *c*-axis. If we inspect the spin down density of states in Figure 12b, we see that a very small flat density of states crosses the Fermi level. Such structure is the result of a strongly dispersive band along the $k_z$ direction in the Brillouin zone. Essentially this is a free-electron-like band that

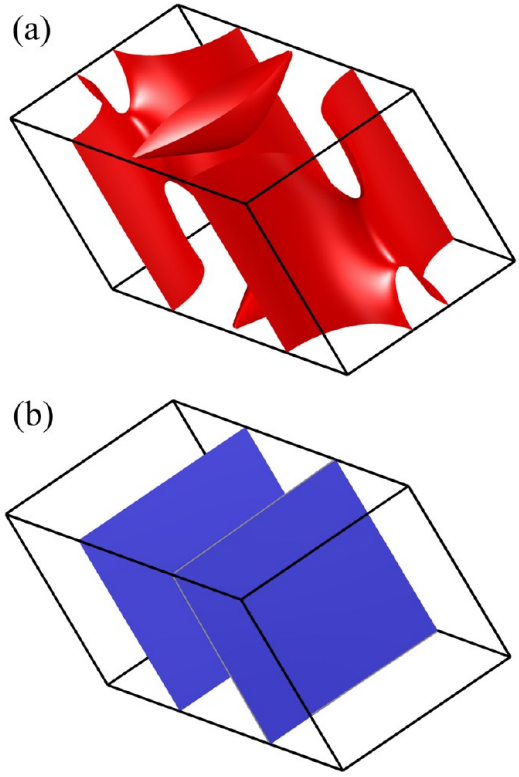


**Figure 13.** $\alpha$-0.125$Li_2O$·$MnO_2$ (a) spin up Fermi surface and (b) spin down Fermi surface.

corresponds to electrons hopping along the *c*-axis via the $Li_2O$ species.

We have also conducted the numerical experiment where we have removed all of the $MnO_2$ species from the $\alpha$-0.125$Li_2O$·$MnO_2$ cell to leave just the $Li_2O$. The resulting DOS is zero at the Fermi level indicating the lack of metallic states. Therefore, the metallic states present in $\alpha$-0.125$Li_2O$·$MnO_2$ are not simply derived from the $Li_2O$ but from their interaction with the bulk $\alpha$-$MnO_2$ structure. The gap in the DOS for the $Li_2O$ chain is small at <0.1 eV and therefore is near to metallizing which is effected by its interaction with the $MnO_2$ wall.

For the structure of $\alpha$-0.125$Li_2O$·$MnO_2$ considered in Figure 12a the $Li_2O$ only occupies the tunnel along the *c*-axis centered on the (0.5,0.5) in-plane position. We have also considered the arrangement where the $Li_2O$ alternate between (0.5,0.5) and (0,0) centered tunnels for successive layers along the *c*-axis. However, we find that this arrangement is higher in energy by 220 meV per $Li_2O$. Even in this arrangement the system is still metallic.

The presence of metallic states has the potential to have an advantageous effect on the properties of $\alpha$-0.125$Li_2O$·$MnO_2$ in battery systems. Facile transport of electrons in Li-ion battery cathodes may increase charge and discharge rates in concert with good ion transport. The presence of metallic states can also facilitate electron delivery to the catalytic reactions underpinning the Li−$O_2$ battery system and is currently under investigation.

## 8. CONCLUSIONS

The present study has used density functional theory to deepen our understanding of the intercalation properties of $\alpha$-$MnO_2$, which are relevant to its potential use as an electrode material


dx.doi.org/10.1021/cm400864n | *Chem. Mater.* 2013, 25, 2515−2526

in rechargeable ion batteries and supercapacitors and as a catalyst in Li−$O_2$ batteries. The primary findings include

**(1) Voltages and Structure:** The observed tetragonal structure of $\alpha$-$MnO_2$ is reproduced and the calculated lithium intercalation voltage of 3.36 V vs Li/$Li^+$ in the dilute limit is consistent with experimental electrochemical measurements. Sodium intercalation is predicted to be thermodynamically favorable in three insertion steps with voltages of 3.34 V, 2.84 V, and 2.19 V vs Na/$Na^+$. These voltages are comparable to, but slightly lower than, those obtained for Li-ion insertion.

**(2) Insertion Sites:** The site energies for Li-ion insertion show that the off-center 8*h* site, near the 2 × 2 tunnel walls, is preferred by Li ions in the dilute limit, but shifts to the 8*h*′ site in $\alpha$-$Li_{0.75}MnO_2$. We suggest that the shift to the 8*h*′ site is motivated by a reduction in the Coulomb repulsion between Li ions. By explicit calculation of the phonon spectrum we suggest that the formation of the $\alpha$-$Li_{0.75}MnO_2$ structure will be accessible at battery operating temperatures. The site energies for Na-ion insertion show that the 8*h* site is preferred in the dilute limit, but then the 8*h*′ site in $\alpha$-$Na_{0.75}MnO_2$. This behavior differs to that of Li-ions in that the 8*h* becomes preferred again when intercalation reaches $\alpha$-$NaMnO_2$. We suggest an explanation for this behavior based upon the differing sizes of the $Li^+$ and $Na^+$ ions.

**(3) Structural Stabilization:** The crystal structures of $\alpha$-$Li_{0.75}MnO_2$ and $\alpha$-$LiMnO_2$ are shown to be strongly distorted, which is likely to be a cause of the structural degradation observed for $\alpha$-$MnO_2$ with electrochemical cycling. The presence of $Li_2O$ within the structure is demonstrated to reduce distortions. This is the basis for the good cycling capacity observed in $\alpha$-$MnO_2$ with small quantities of $Li_2O$ and demonstrates a mechanism for the stabilization of lithium battery cathodes during intercalation. In contrast, the presence of $Na_2O$ is found to be less effective in reducing the distortion of the crystal structure in the presence of intercalated sodium.

**(4) Ion Migration:** Lithium migration barriers in $\alpha$-$MnO_2$ are calculated to be <0.3 eV in the dilute limit, but the dominant migration path for $\alpha$-$Li_{0.75}MnO_2$ possesses a higher barrier of 0.55 eV, which is of relevance to its rate performance. Similar behavior is found for sodium with the dominant pathway in $\alpha$-$Na_{0.75}MnO_2$ possessing a migration barrier of 0.48 eV, indicating that despite the larger size of the sodium ion it may achieve comparable diffusion to lithium. The low diffusion barriers in the dilute limit may be important to the reaction kinetics when $\alpha$-$MnO_2$ is used as an electrocatalyst.

**(5) $Li_2O$ Incorporation and Electronic Conductivity:** The electronic density of states in $\alpha$-$MnO_2$ with the incorporation of $Li_2O$ has the character of a full metal and not a half-metal as suggested previously. This may be key to its high activity as a catalyst in Li−$O_2$ batteries and relevant to its performance as supercapacitor electrodes.

## AUTHOR INFORMATION


### Corresponding Author

*E-mail: dt331@bath.ac.uk (D.A.T.); m.s.islam@bath.ac.uk (M.S.I.).


### Notes

The authors declare no competing financial interest.

## ACKNOWLEDGMENTS

We are grateful to Peter G. Bruce and Grahame Gardiner for discussions, the EPSRC for funding (EP/H019596; EP/H003819), and the Materials Chemistry Consortium for Hector supercomputer resources.

## REFERENCES


(1) Tarascon, J.-M.; Delacourt, C.; Prakash, A. S.; Morcrette, M.; Hegde, M. S.; Wurm, C.; Masquelier, C. *Dalton Trans.* **2004**, 2988−2994.
(2) Ellis, B. L.; Lee, K. T.; Nazar, L. F. *Chem. Mater.* **2010**, *22*, 691.
(3) Goodenough, J. B.; Kim, Y. *Chem. Mater.* **2010**, *22*, 587.
(4) Whittingham, M. S.; Savinell, R. F.; Zawodzinski, T. *Chem. Rev.* **2004**, *104*, 4243−4244.
(5) Armstrong, A. R.; Bruce, P. G. *Nature* **1996**, *381*, 499−500.
(6) Tarascon, J.-M.; Wange, E.; Shokoohi, F. K.; McKinnon, W. R.; Colson, S. *J. Electrochem. Soc.* **1991**, *138*, 2859−2864.
(7) Thackeray, M. M. *Prog. Solid State Chem.* **1997**, *25*, 1−71.
(8) Armstrong, A. R.; Holzapfel, M.; Novak, P.; Johnson, C. S.; Kang, S. H.; Thackeray, M. M.; Bruce, P. G. *J. Am. Chem. Soc.* **2006**, *128*, 8694−8698.
(9) Balachandran, D.; Morgan, D.; Ceder, G.; van de Walle, A. *J. Solid State Chem.* **2003**, *173*, 462−475.
(10) Chabre, Y.; Pannetier, J. *Prog. Solid State Chem.* **1995**, *23*, 1.
(11) Kim, C.-H.; Akase, Z.; Zhang, L.; Heuer, A. H.; Newman, A. E.; Hughes, P. J. *J. Solid State Chem.* **2006**, *179*, 753−774.
(12) Johnson, C. S.; Dees, D. W.; Mansuetto, M. F.; Thackeray, M. M.; Vissers, D. R.; Argyriou, D.; Loong, C. K.; Christensen, L. *J. Power Sources* **1997**, *68*, 570−577.
(13) Johnson, C. S.; Thackeray, M. M. *J. Power Sources* **2001**, *97*−*8*, 437−442.
(14) Johnson, C. S. *J. Power Sources* **2007**, *165*, 559−565.
(15) Xing, L.; Cui, C.; Ma, C.; Xue, X. *Mater. Lett.* **2011**, *65*, 2104−2106.
(16) Kadoma, Y.; Akahira, T.; Fukuda, T.; Ui, K.; Kumagai, N. *Funct. Mater. Lett.* **2012**, *5*, 1250004.
(17) Li, B.; Rong, G.; Xie, Y.; Huang, L.; Feng, C. *Inorg. Chem.* **2006**, *45*, 6404−6410.
(18) Li, L.; Nan, C.; Lu, J.; Peng, Q.; Li, Y. *Chem. Commun.* **2012**, *48*, 6945.
(19) Yang, Y.; Xiao, L.; Zhao, Y.; Wang, F. *Int. J. Electrochem. Sci.* **2008**, *3*, 67.
(20) Cheng, F.-Y.; Zhao, J.-Z.; Song, W.; Li, C.-S.; Ma, H.; Chen, J.; Shen, P.-W. *Inorg. Chem.* **2006**, *45*, 2038−2044.
(21) Kijima, N.; Takahashi, Y.; Akimoto, J.; Awaka, J. *J. Solid State Chem.* **2005**, *178*, 2741−2750.
(22) Hill, L. I.; Verbaere, A.; Guyomard, D. *J. Power Sources* **2003**, *119*−*121*, 226−231.
(23) Xu, M.; Kong, L.; Zhou, W.; Li, H. *J. Phys. Chem. C* **2007**, *111*, 19141−19147.
(24) Lang, X.; Hirata, A.; Fujita, T.; Chen, M. *Nat. Nanotechnol.* **2011**, *6*, 232−236.
(25) Devaraj, S.; Munichandraiah, N. *J. Phys. Chem. C* **2008**, *112*, 4406−4417.
(26) Wang, Y.-T.; Lu, A.-H.; Zhang, H.-L.; Li, W.-C. *J. Phys. Chem. C* **2011**, *115*, 5413−5421.
(27) Devaraj, S.; Gabriel, G. S.; Gajjela, S. R.; Balaya, P. *Electrochem. Solid State Lett.* **2012**, *15*, A57−A59.
(28) Debart, A.; Paterson, A. J.; Bao, J.; Bruce, P. G. *Angew. Chem., Int. Ed.* **2008**, *47*, 4521−4524.
(29) Thapa, A. K.; Ishihara, T. *J. Power Sources* **2011**, *196*, 7016.
(30) Freunberger, S. A.; Chen, Y.; Peng, Z.; Griffin, J. M.; Hardwick, L. J.; Bardé, F.; Novák, P.; Bruce, P. G. *J. Am. Chem. Soc.* **2011**, *133*, 8040−8047.
(31) McCloskey, B. D.; Scheffler, R.; Speidel, A.; Bethune, D. S.; Shelby, R. M.; Luntz, A. C. *J. Am. Chem. Soc.* **2011**, *133*, 18038−18041.
(32) Delmas, C.; Bracconnier, J. J.; Fouassier, C.; Hagenmuller, P. *Solid State Ionics* **1981**, *3*−*4*, 165.
(33) Doeff, M. M.; Richardson, T. J.; Kepley, L. *J. Electrochem. Soc.* **1996**, *143*, 2507.
(34) Palomares, V.; Serras, P.; Villaluenga, I.; Hueso, K. B.; Carretero-Gonzalez, J.; Rojo, T. *Energy Environ. Sci.* **2012**, *5*, 5884.

(35) Doeff, M. M.; Peng, M. Y.; Ma, Y.-P.; DeJonghe, L. C. *J. Electrochem. Soc.* **1994**, *141*, L145−L147.
(36) Sauvage, F.; Laffont, L.; Tarascon, J.-M.; Baudrin, E. *Inorg. Chem.* **2007**, *46*, 3289−3294.
(37) Tevar, A. D.; Whitacre, J. F. *J. Electrochem. Soc.* **2010**, *157*, A870−A875.
(38) Cao, Y.; Xiao, L.; Wang, W.; Choi, D.; Nie, Z.; Yu, J.; Saraf, L. V.; Yang, Z.; Liu, J. *Adv. Mater.* **2011**, *23*, 3155−3160.
(39) Lee, J.-H.; Black, R.; Popov, G.; Pomerantseva, E.; Nan, F.; Botton, G. A.; Nazar, L. F. *Energy Environ. Sci.* **2012**, *5*, 9558.
(40) Zhang, R.; Yu, X.; Nam, K.-W.; Ling, C.; Arthur, T. S.; Song, W.; Knapp, A. M.; Ehrlich, S. N.; Yang, X.-Q.; Matsui, M. *Electrochem. Commun.* **2012**, *23*, 110.
(41) Rasul, S.; Suzuki, S.; Yamaguchi, S.; Miyayama, M. *Electrochim. Acta* **2012**, *82*, 243−249.
(42) Maphanga, R. R.; Sayle, D. C.; Sayle, T. X. T.; Ngoepe, P. E. *Phys. Chem. Chem. Phys.* **2011**, *13*, 1307.
(43) Sayle, T. X. T.; Maphanga, R. R.; Ngoepe, P. E.; Sayle, D. C. *J. Am. Chem. Soc.* **2009**, *131*, 6161−6173.
(44) Sayle, T. X. T.; Catlow, C. R. A.; Maphanga, R. R.; Ngoepe, P. E.; Sayle, D. C. *J. Cryst. Growth* **2006**, *294*, 118−129.
(45) Sayle, T. X. T.; Catlow, C. R. A.; Maphanga, R. R.; Ngoepe, P. E.; Sayle, D. C. *J. Am. Chem. Soc.* **2005**, *127*, 12828−12837.
(46) Sayle, T. X. T.; Ngoepe, P. E.; Sayle, D. C. *ACS Nano* **2009**, *3*, 3308−3314.
(47) Ling, C.; Mizuno, F. *Chem. Mater.* **2012**, *24*, 3943.
(48) Cockayne, E.; Li, L. *Chem. Phys. Lett.* **2012**, *544*, 53−58.
(49) Trahey, L.; Karan, N. K.; Chan, M. K. Y.; Lu, J.; Ren, Y.; Greeley, J.; Balasubramanian, M.; Burrell, A. K.; Curtiss, L. A.; Thackeray, M. M. *Adv. Energy Mater.* **2013**, *3*, 75−84.
(50) Kim, H.; Kim, D. J.; Seo, D.-H.; Yeom, M. S.; Kang, K.; Kim, D. K.; Jung, Y. *Chem. Mater.* **2012**, *24*, 1205.
(51) Perdew, J. P.; Burke, K.; Ernzerhof, M. *Phys. Rev. Lett.* **1996**, *77*, 3865.
(52) Zhou, F.; Cococcioni, M.; Marianetti, C. A.; Morgan, D.; Ceder, G. *Phys. Rev. B* **2004**, *70*, 235121.
(53) Kresse, G.; Furthmüller, J. *Phys. Rev. B* **1996**, *54*, 11169−11186.
(54) Anisimov, V. I.; Gunnarsson, O. *Phys. Rev. B* **1991**, *43*, 7570−7574.
(55) Madsen, G. K. H.; Novak, P. *Europhys. Lett.* **2005**, *69*, 777.
(56) Antonides, E.; Janse, E. C.; Sawatzky, G. A. *Phys. Rev. B* **1977**, *15*, 1669−1679.
(57) Anisimov, V. I.; Zaanen, J.; Andersen, O. K. *Phys. Rev. B* **1991**, *44*, 943−954.
(58) Tompsett, D. A.; Middlemiss, D. S.; Islam, M. S. *Phys. Rev. B* **2012**, *86*, 205126.
(59) Eames, C.; Armstrong, A. R.; Bruce, P. G.; Islam, M. S. *Chem. Mater.* **2012**, *24*, 2155.
(60) Shannon, R. D. *Acta Crystallogr., Sect. A* **1976**, *32*, 751.
(61) Togo, A.; Oba, F.; Tanaka, I. *Phys. Rev. B* **2008**, *78*, 134106.
(62) Rossouw, M. H.; Liles, D. C.; Thackeray, M. M.; David, W. I. F.; Hull, S. *Mater. Res. Bull.* **1992**, *27*, 221−230.
(63) Kijima, N.; Sakata, Y.; Takahashi, Y.; Akimoto, J.; Kumagai, T.; Igarashi, K.; Shimizu, T. *Solid State Ionics* **2009**, *180*, 616−620.
(64) Grau-Crespo, R.; Hamad, S.; Catlow, C. R. A.; de Leeuw, N. H. *J. Phys.: Condens. Matter* **2007**, *19*, 256201.
(65) Dalton, A. S.; Belak, A. A.; Van der Ven, A. *Chem. Mater.* **2012**, *24*, 1568−1574.
(66) Kanoh, H.; Feng, Q.; Miyai, Y.; Ooi, K. *J. Electrochem. Soc.* **1995**, *142*, 702.
(67) Islam, M. S.; Driscoll, D. J.; Fisher, C. A. J.; Slater, P. R. *Chem. Mater.* **2005**, *17*, 5085−5092.
(68) Tompsett, D. A.; Parker, S. C.; Bruce, P. G.; Islam, M. S. *Chem. Mater.* **2013**, *25*, 536.
(69) Tompsett, D. A.; Yin, Z. P.; Lonzarich, G. G.; Pickett, W. E. *Phys. Rev. B* **2010**, *82*, 235101.
(70) Tompsett, D. A.; Needs, R. J.; Grosche, F. M.; Lonzarich, G. G. *Phys. Rev. B* **2010**, *82*, 155137.
(71) Tompsett, D.; Lonzarich, G. *Phys. B: Condens. Matter* **2010**, *405*, 2440.